Materials Characterization 120 (2016) 268–272

Contents lists available at ScienceDirect

Materials Characterization

journal homepage: www.elsevier.com/locate/matchar

Atom probe tomography of intermetallic phases and interfaces formed in dissimilar joining between Al alloys and steel

B. Lemmens [a,b], H. Springer [c,*], M.J. Duarte [c], I. De Graeve [a,b], J. De Strycker [d], D. Raabe [c], K. Verbeken [a]

[a] Department of Materials Science and Engineering, Ghent University (UGent), Technologiepark 903, B-9052 Zwijnaarde, Belgium
[b] Research group of Electrochemical and Surface Engineering (SURF), Vrije Universiteit Brussel (VUB), Pleinlaan 2, B-1050 Brussels, Belgium
[c] Max-Planck-Institut für Eisenforschung GmbH, D-40237 Düsseldorf, Germany
[d] ArcelorMittal Global R&D Gent, J.F. Kennedylaan 3, B-9060 Zelzate, Belgium

ARTICLE INFO

Article history:
Received 29 April 2016
Received in revised form 7 September 2016
Accepted 9 September 2016
Available online 10 September 2016

Keywords:
Steel
Aluminium
Intermetallics
Hot dip aluminizing
Welding

ABSTRACT

While Si additions to Al are widely used to reduce the thickness of the brittle intermetallic seam formed at the interface during joining of Al alloys to steel, the underlying mechanisms are not clarified yet. The developed approach for the site specific atom probe tomography analysis revealed Si enrichments at grain and phase boundaries between the θ (Fe_4Al_{13}) and η (Fe_2Al_5) phase, up to about ten times that of the concentration in Al. The increase in Si concentration could play an important role for the growth kinetics of the intermetallic phases formed for example in hot-dip aluminizing of steel.

1. Introduction

Dissimilar joining of iron (Fe), or steel, and aluminium (Al) alloys is of key technological relevance, as it allows combining the high strength of the former with the superior corrosion resistance (especially at elevated temperatures), high thermal conductivity and high reflectivity of the latter in one hybrid part [1]. Joining by thermal processes is of special interest as it creates a close metallic bond between both materials, typically offering high strength levels, good heat- and electrical conductivity and a large, leak-proof bonding area with minimised stress concentrating geometries [2]. Consequently, numerous joining techniques with various thermal processes have been developed, reflecting the wide range of applications for dissimilar joints of these most commonly used structural materials [3]. Brazed joints for example are found in domestic appliances such as cooking pans or water boilers [4], whereas laser-based procedures aim at joining sheet material for transportation systems [5]. An undesired joining is found during casting of Al, where die soldering can occur as an interaction between the casting alloy and the steel die [6]. Hot dip aluminizing (HDA), i.e. immersing steel into a molten Al bath, is used to coat large surfaces of steel [7] and is now increasingly used replacing zinc (Zn) coatings. Al compared to Zn offers the advantage of improved weldability and exhibits an increased oxidation resistance at elevated temperatures [8]. The latter is exploited in the direct hot stamping operations of high strength steel sheets into highly mechanically loaded automotive chassis components, where the Al-based coating minimises surface oxidation and decarburization [9].

The main challenge in all these joining procedures is the formation of inherently brittle intermetallic phases (IMP) at the interface between Al alloys and steel as a consequence of the temperature induced interdiffusion which may drastically reduce the joint performance [10]. Additional to the θ phase (Fe_4Al_{13}) neighbouring the Al-based coating, the η phase (Fe_2Al_5) adjacent to steel is the dominant component of the IMP seam, as it grows the fastest following parabolic kinetics [11–15], caused by accelerated diffusion along its [001] direction [16]. To improve the joint properties (e.g. the formability of a coated sheet), up to 12 wt.% of silicon (Si) is commonly added to Al, as it effectively minimises the IMP thickness via suppressing the growth of the η-phase [17–19]. The underlying phenomena for this growth retardation, however, are not fully clarified yet [6,17,20–25]. While for example Nicholls [20] proposed an interaction of Si atoms with the open crystallographic arrangement of the η phase, other hypotheses suggest a reduction of the activation energy [22,23], the formation of a ternary chemical compound acting as a diffusion barrier [24], or a reduced activity of Al [6,25]. This uncertainty is partly related to the complex characterisation of reaction zones in dissimilar joining of Al and steel, i.e. investigating brittle hard phases formed as micro- and submicrometric compounds, whose structural and especially chemical nature are difficult to assess.

* Corresponding author.
E-mail address: h.springer@mpie.de (H. Springer).

http://dx.doi.org/10.1016/j.matchar.2016.09.008
1044-5803/

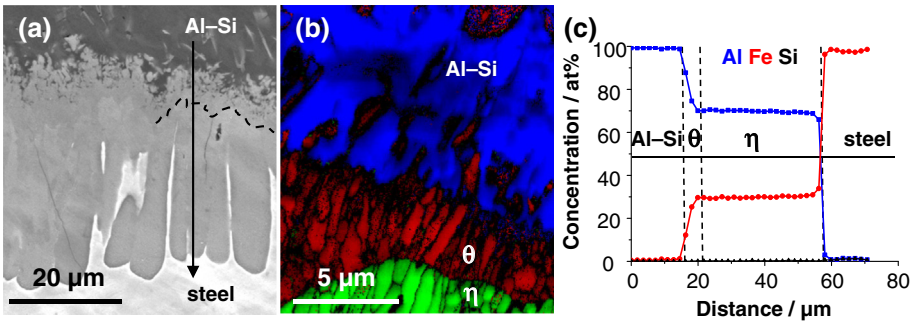

Fig. 1. SEM investigation of the interface region between steel and solidified Al—Si coating: (a) overview of the characteristic intermetallic phase seam (b) EBSD phase map revealing the θ phase layer located between the η phase and Al, (c) EDX line scan result obtained along the arrow in (a).

2. Objective

Hence we demonstrate on the example of steel coated by HDA, how the chemical nature of the IMP seam can be investigated at atomic resolution by an adapted methodology for atom probe tomography (APT) regarding targeted sample preparation and analysis parameters. Focussing on the Si distribution within the θ and η phases, especially at the respective interfaces, we aim at contributing to a better understanding of the role of Si in dissimilar joining of Al with steel and outline future research opportunities.

3. Materials and Methods

HDA samples were prepared with a Rhesca® hot dip simulator by immersing a 1.2 mm thick low carbon steel (0.04 wt.% C; European grade DC06), under a reducing atmosphere (nitrogen with 5 vol.% hydrogen), in an Al bath containing 0.3 wt.% Si and 3 wt.% Fe (0.29 at.% Si and 1.47 at.% Fe). This bath composition was chosen to be able to trace the Si distribution within the IMP seam without ternary Al—Fe—Si phases forming at higher Si concentrations [26], while the saturation of the bath with Fe confines the dissolution of the steel to a minimum [13]. Prior to dipping the steel sheet was preheated to 800 °C for 60 s. Immersion was performed for 60 s at a bath temperature of 680 °C. Finally, the aluminized sheet was removed from the bath and cooled to room temperature with nitrogen gas wiping.

Scanning electron microscopy (SEM) investigations were performed with a FEG SEM Quanta 450 equipped with a field emission gun, EDAX energy dispersive X-ray spectroscopy (EDX) system and a TSL electron backscatter diffraction (EBSD) system. The specimens for APT investigations were prepared based on the established focused ion beam (FIB; FEI Helios Nanolab 600i) methodology detailed elsewhere [27]. APT measurements were performed using a local electrode atom probe (Imago LEAP™ 3000X HR) operated in laser mode under ultra-high vacuum to improve the data yield. The experimental parameters were set as follows: set point temperature of 60 K, pulse repetition rate of 250 kHz, laser energy of 0.2 nJ and a detection rate of 0.01 atoms per pulse. Besides the elements of interest (Al, Fe and Si) impurities of Ti, N and Cr were found in concentrations below 0.01 at.% and H was present with a concentration of 1 at.%. The APT data was reconstructed and analyzed within the framework of the IVAS® software. The peak decomposition of the mass spectra was based on the natural abundance of the different isotopes, while the background is considered from the local range-assisted background model [32].

4. Results

The cross section of a coated steel is depicted in Fig. 1a, the reaction zone formed between the Al-based coating (top) and steel (bottom) shows the well-known microstructure found in such joining/interdiffusion conditions [12,13,22,28]. According to the EBSD investigations (Fig. 1b) the IMP seam with a total thickness of 50 µm consists mainly of the η phase, protruding in a finger-like manner into the steel, and a much thinner θ phase layer with a finely serrated interface towards the Al-based coating. The interface between θ and η phase is irregular and deviates from a planar surface about ±5 µm. The Al concentrations in the θ and η phase according to EDX (Fig. 1c) are about 75 and 70 at.%, respectively, in good agreement with literature data [22]. The low amount of Si did not allow for a reliable quantification of Si in the IMP seam via SEM EDX.

Targeted APT investigations of the interface between θ and η phase, which is of special interest for elucidating the role of Si, were prepared as sketched in Fig. 2. A triangular bar along the θ/η interface was cut out from a polished cross section and placed on Si tips. Annular milling from the top view resulted in needle-like APT specimens (thickness ~100 nm, length ~500 nm, tip radius ~30 nm) with the θ/η interface along the longitudinal axis of the tip. Final milling with the energy reduced to 5 keV ensured a Ga content below 0.007 at.% in the analyzed regions. This kind of sample manufacturing may result in the preparation of specimens that are located within single phase regions due to the irregular geometry of the interface, which is much larger than the thickness of an APT tip. As shown in Figs. 1 and 2, the θ/η interface is additionally difficult to observe and target for site-specific APT tip extraction due to the weak contrast among these chemically similar phases. The probability of targeting the interface within the APT needle can be increased by preparing the specimens with the θ/η interface perpendicular to the APT evaporation direction. This is achievable by a rotation of

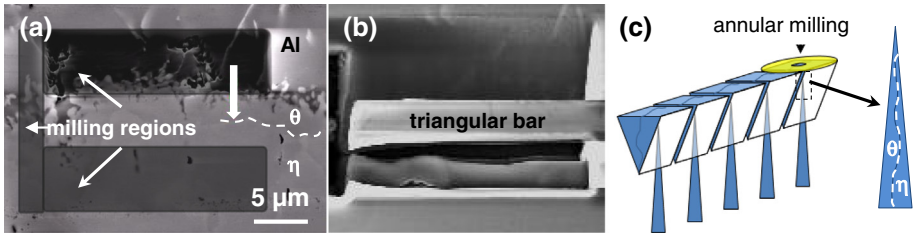

Fig. 2. FIB procedure for targeted sample preparation of the interface between η and θ phase: (a) cross section view with indicated areas for milling, (b) obtained triangular bar containing the interface region, and (c) sketch of the preparation of the atom probe needles from the triangular bar by annular milling.

the extracted bar prior to annular milling; however, this preparation generates specimens which are more susceptible to fracture when the evaporating zone reaches the θ/η interface. This enhanced fracture can be explained by the inherent weakness of this phase boundary [10] which is additionally affected by an increased Ga implementation through the more complex and longer FIB operation needed to achieve the rotation of the bar [29].

Fig. 3 shows the colour-coded qualitative 2 dimensional concentration plots of Al, Fe and Si, obtained from a slice of 3 nm thickness along the analysis direction of an APT reconstruction successfully targeting the θ/η interface. The Al-enriched (and consequently decreased in Fe) regions at the top and the bottom of the tip correspond to the θ phase. The η phase, with lower Al content, is located in between these θ phases. Single phase regions appear to be chemically homogeneous apart from the well-known APT trajectory aberrations causing lines with high or low hit density on the detector around crystallographic poles along the tip axis [30]. Si is enriched at the phase boundaries between θ and η as well as on plate-like features within the η phase (identified according to their chemistry as TiN). The derived compositions of the single phase regions are listed in Table 1. Earlier investigations [31] showed that the APT measured compositions in Fe—Al intermetallics are affected by the overlapping peaks of the $^{27}Al^{+}$ and $^{54}Fe^{2+}$ at 27 Da. A second peak overlap appears here at 28 Da, stemming from $^{56}Fe^{2+}$ and $^{28}Si^{+}$. However, in the present measurements the respective concentrations are not significantly affected (typically less than 1 at.%) by decomposing the overlapping peaks, and considering single or all hits, as shown in Table 1. In Fig. 4 an exemplary mass-spectrum of an η/η grain boundary is shown. Due to enlarged thermal tails, the error associated with the concentration of Si is about 10%. The derived compositions (all hits, decomposed) of about 73.33 Al, 26.20 Fe and 0.47 Si for the η phase, as well as 75.92 Al, 23.73 Fe and 0.35 Si for θ phase (all in at.%), are in good agreement with the SEM-EDX data (Fig. 1), allowing to differentiate between both phases in the reconstructed APT data. The *Si*-concentration in the η phase is with 0.47 at.% slightly higher than in the θ phase (0.35 at.%). This relative concentration difference is in agreement with literature data [22], and both values are below the solubility limit of Si, which is reported to be about 1–2 at.% [33].

The three APT reconstructions shown in Fig. 5a give examples of single phase θ and η regions (and their respective grain boundaries), as well as from θ/η interfaces. The grey regions indicate isoconcentration surfaces with 1.5 at.% Si. Iso-concentration surfaces are used only for visualization in this overview, as the low concentration of Si atoms and the different orientations of the interfaces within the same reconstruction make it difficult to highlight these zones with using atom maps. In addition, small titanium (Ti) rich inclusions, below 30 nm size, were found within the η phase regions, highlighted by black isoconcentration surfaces of 2 at.% Ti. These are likely to be Ti-nitrides, stemming from the steel, where 0.04 at.% Ti is alloyed for capturing interstitial elements such as nitrogen to eliminate bake-hardening effects (strengthening through formation of Cottrel atmospheres at elevated temperature) [37].

Table 1
Normalized compositions in at.% of the η and θ phase.

			Al	Fe	Si
η	Single hits	Decomposed	73.46	25.71	0.83
		Not decomposed	73.32	26.30	0.38
	All hits	Decomposed	73.33	26.20	0.47
		Not decomposed	71.76	27.78	0.45
θ	Single hits	Decomposed	75.52	24.07	0.41
		Not decomposed	74.77	24.76	0.47
	All hits	Decomposed	75.92	23.73	0.35
		Not decomposed	75.90	23.81	0.29

Figs. 5 b-d display selected atom maps of Fe, Al and Si across different interfaces, while the insets show the analyzed region depicting only the Si atoms as grey dots. The concentration profiles across a θ/θ (Fig. 5b) and an η/η (Fig. 5c) grain boundaries reveal an increase of the *Si*-concentration up to 1.5 and 3 at.%, respectively. At the interface between the θ and η phase (Fig. 5d) a similar enrichment in Si to the η/η grain boundary of about 3 at.% is observed. The difference in the width of the interfaces and the broadening of the Si-peaks can be attributed to tomographic artifacts such as the local magnification effect (especially pronounced in interfaces parallel to the analysis direction [34]) and to the curvature of the analyzed interfaces. Therefore, these enrichments are quantified by the atomic interfacial excess (i.e. the ratio of the atomic excess obtained from the plot over the analyzed interfacial area), calculated in this work according to a previously reported method [35,36]. An example of this calculation results is given in Fig. 6 for an η/η grain boundary. Here an excess of about 5 at nm^{-2} was calculated, while the interfacial excesses of the θ/θ and θ/η boundaries account for about 2 and 3 at nm^{-2}, respectively.

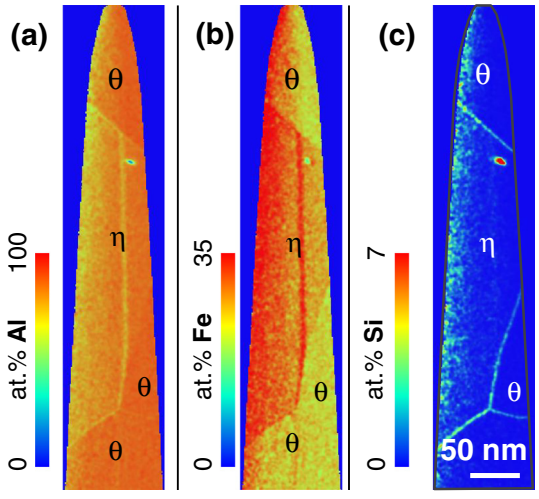

Fig. 3. 2 dimensional concentration plots of Al (a), Fe (b) and Si (c), obtained from a 3 nm thick slice along the evaporation direction of a tomographic reconstruction of an APT specimen. The difference between Al and Fe concentrations allows distinguishing between η and θ phase regions.

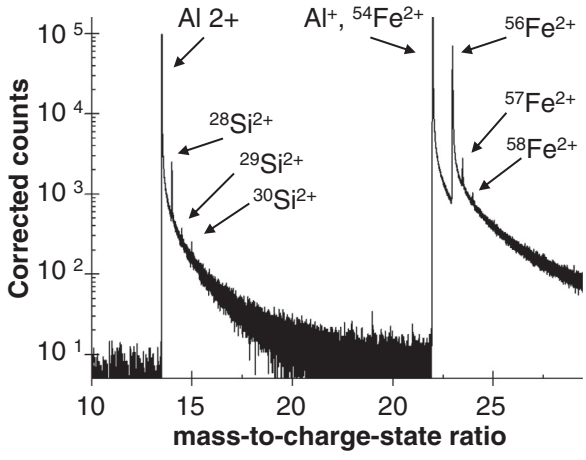

Fig. 4. Exemplary mass spectrum from a region surrounding an η/η grain boundary.

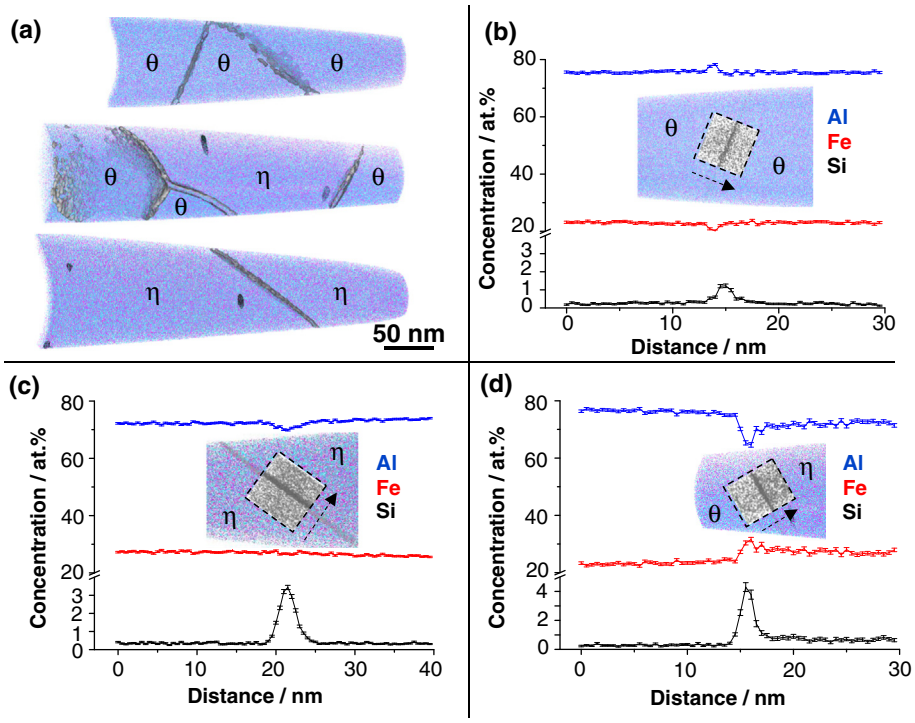

Fig. 5. Atom probe results for three different 3 dimensional reconstructions: (a) overview showing Si enrichment at interfaces and inclusions. (b-d) concentration profiles across a grain boundary within the θ phase, a grain boundary within the η phase and the θ/η interface, respectively. The insets show the respective atom maps, highlighting only the Si atoms in the analyzed regions of interest.

5. Discussion

Despite the rather straightforward experimental setup required to probe interdiffusion between steel and Al alloys and the amount of research devoted to it due to its engineering relevance for dissimilar joining, the role of Si in the growth retardation of IMP is still not clear [6,17,20–25]. Our results suggest that the observed enrichment of Si at the grain boundaries of the IMP and especially at the θ/η interface may play an important role in the suppression of the otherwise extremely rapid growth kinetics of the η phase [16]. While we obtained IMP seams of similar thickness as experiments using pure Al [13,28] due to the rather low *Si*-concentration in the Al bath, the already observed Si-enriched zones (to more than a factor 10 compared to the concentration in the Al bath based on the approximated concentration values) may act as a diffusion barrier for Al atoms at higher Si-concentrations in the Al bath. Following the approach presented involving APT analysis, future experiments can be efficiently conducted, investigating the relationship between localized concentration and growth suppression as a function of the Si content within Al, especially in the technological relevant range between 3 and 10 wt.% Si. Special emphasis should be laid, for higher Si contents, on the then additional formation of the ternary Al—Fe—Si phases, as well as on the case of interdiffusion below the liquidus temperature of the Al—Si alloys, where Si was observed to have the opposite effect, i.e. resulting in a growth acceleration of the IMP seam rather than retarding it [22].

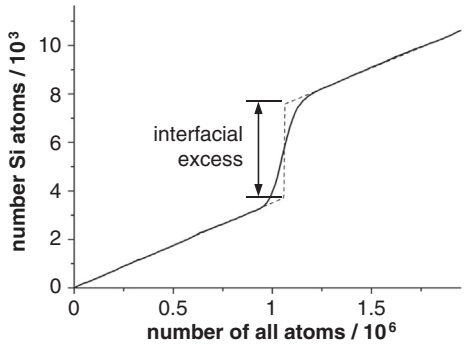

Fig. 6. Cumulative diagram exemplifying how the interfacial excess was determined for Si at an η/η grain boundary.

Acknowledgements

Financial support through the Special Research Fund (BOF), Ghent University (BOF10/ZAP/121) is gratefully acknowledged. A. Szczepaniak and P. Kürnsteiner are acknowledged for assistance with FIB, SEM and APT analysis.

References

[1] M.F. Ashby, Materials Selection in Mechanical Design, Butterworth-Heinemann, Burlington, MA, USA, 2005.
[2] U. Dilthey, L. Stein, Sci. Technol. Weld. Join. 11 (2006) 135.
[3] T.A. Barnes, I.R. Pashby, J. Mater. Process. Technol. 99 (2000) 62–71.
[4] M. Roulin, J. Luster, G. Karadeniz, A. Mortensen, Weld J Suppl 78 (1999) 151–155.
[5] A. Szczepaniak, J. Fan, A. Kostka, D. Raabe, Adv. Eng. Mater. 14 (7) (2012) 464–472.
[6] S. Shankar, D. Apelian, Metall. Mater. Trans. A 33B (2002) 465–476.
[7] V.R. Ryabov, Aluminizing of Steel, Oxonian Press, New Delhi, 1985.
[8] C.-J. Wang, S.-M. Chen, Surf. Coat. Technol. 200 (2006) 6601–6605.
[9] H. Karbasian, A.E. Tekkaya, J. Mat, Process Technol 210 (2010) 2103–2118.
[10] H. Springer, A. Kostka, J.F. dos Santos, D Raabe Mat Sci Eng A 528 (2011) 4630.
[11] K. Bouche, F. Barbier, A. Coulet, Mater. Sci. Eng. A249 (1998) 167–175.
[12] A. Bouayad, C. Gerometta, A. Belkebir, A. Ambari, Mater. Sci. Eng. A363 (2003) 53–61.
[13] G. Eggeler, W. Auer, H. Kaesche, Z. Metallkde, Bd 77 (1986) 239–244.
[14] D. Naoi, M. Kajihara, Mater. Sci. Eng. A459 (2007) 375–382.
[15] F. Barbier, D. Manuelli, K. Bouché, Scr. Mater. 36 (4) (1997) 425–431.
[16] T. Heumann, S. Dittrich, Z Metall 50 (1959) 617–625.
[17] M.V. Akdeniz, A.O. Mekhrabov, T. Yilmaz, Scr. Mater. 31 (12) (1994) 1723–1728.
[18] M.A. Shady, A.R. El-Sissi, A.M. Attia, J. Mater. Sci. Lett. 15 (1996) 1032–1036.
[19] G. Eggeler, W. Auer, H. Kaesche, J. Mater. Sci. 21 (1986) 3348–3350.
[20] J.E. Nicholls, Anti-Corros Methods Mater 11 (10) (1964) 16–21.
[21] E. Gebhardt, W Obrowski Z Metall 44 (1953) 154.
[22] H. Springer, A. Kostka, E.J. Payton, D. Raabe, A. Kaysser-Pyzalla, G Eggeler Acta Mater 59 (2010) 1586.

[23] F.-C. Yin, M.-X. Zhao, Y.-X. Liu, W. Han, Z. Li, Trans. Nonferrous Metals Soc. China 23 (2013) 556–561.
[24] A.K. Kurakin, Phys. Met. Metallogr. 30 (1970) 108–114.
[25] K. Zhang, X. Bian, Y. Li, Y. Liu, C. Yang, J. Mater, Restor. Dent. 28 (23) (2013) 3279–3328.
[26] N. Krendelsberger, F. Weitzer, J.C. Schuster, Metall Mat Trans A 38 (2007) 1681.
[27] K. Thompson, D. Lawrence, D.J. Larson, J.D. Olson, T.F. Kelly, B. Gorman, Ultramicroscopy 107 (2007) 131–139.
[28] W.-J. Cheng, C.-J. Wang, Surf. Coat. Technol. 204 (2009) 824–828.
[29] M.K. Miller, K.F. Russell, K. Thompson, R. Alvis, D.J. Larson, Microsc. Microanal. 13 (2007) 428–436.
[30] B. Gault, M.P. Moody, J.M. Cairney, S.P. Ringer, Mater Today 15 (9) (2012) 378–386.
[31] R.K.W. Marceau, A.V. Ceguerra, A.J. Breen, D. Raabe, S.P. Ringer, Ultramicroscopy 157 (2015) 12–20.
[32] B. Gault, M.P. Moody, J.M. Cairney, S.P. Ringer, Atom probe Microscopy, Springer Series in Mater Sci 160 (2012).
[33] V.G. Rivlin, G.V. Raynor, Int Met Rev 26 (1981) 133–152.
[34] F. Vurpillot, A. Cerezo, D. Blavette, D.J. Larson, Microsc. Microanal. 10 (2004) 384–390.
[35] B.W. Krakauer, D.N. Seidman, Phys. Rev. B 48 (9) (1993) 6724–6729.
[36] P.J. Felfer, C.R. Killmore, J.G. Williams, K.R. Carpenter, S.P. Ringer, J.M. Cairney, Acta Mater. 60 (2012) 5049–5055.
[37] H. Berns, W. Theisen, Eisenwerkstoffe: Stahl und Gusseisen, Springer Verlag, Berlin, Heidelberg, 2006.